

1 INTRODUCTION

2 Above Earth's atmosphere are the Van Allen radiation belts, a toroidally-shaped
3 pair of belts that consist of a complex and dynamic plasma environment. The inner
4 radiation belt is stable, consists of mostly energetic protons, and is located within 2
5 Earth radii (measured near the equator) above Earth's surface. The outer radiation
6 belt, on the other hand, consists of mostly energetic electrons, is highly dynamic
7 on day and hour time scales, and is typically found between 4 and 8 Earth radii
8 above Earth's surface. These belts pose a threat to space exploration due to their
9 adverse effects on our bodies and electrical components. A few **effects** include: a
10 high radiation dose for manned missions, degradation of silicon that causes transistor
11 malfunction, computer memory corruption due to bit flips, etc. With these effects in
12 mind, it is no surprise that the radiation belts have been extensively studied since
13 their discovery in the 1960s.

14 The radiation belt particles, mostly consisting of electrons and protons, are at
15 times unstable to wave growth and generate electric and magnetic waves. These
16 waves can then accelerate and scatter radiation belt particles with a variety of wave-
17 particle mechanisms. These wave-particle interactions are believed to be responsible
18 for scattering electron microbursts, a short and intense increase of precipitating
19 electrons into Earth's atmosphere, that are capable of destroying ozone molecules
20 and rapidly deplete the outer belt's electrons.

21 Electron microbursts, henceforth referred to as microbursts, are typically
22 observed by low Earth orbiting spacecraft, sounding rockets, and high altitude
23 balloons as a sub-second impulse of electrons. Some of the most intense microbursts
24 have electron fluxes that are a factor of 10 to 100 above the background (for example
25 see Fig. 7 in Blake et al. (1996)). Since they were first reported by Anderson and

26 Milton (1964), the intense transient nature of microbursts have compelled countless
 27 researchers to pursue an understanding of their properties, their effects on the
 28 environment, and the physical mechanism(s) that create microbursts. Microbursts
 29 are widely believed to be created by wave-particle scattering between a plasma wave
 30 called whistler mode chorus and outer radiation belt electrons, although many details
 31 regarding the scattering mechanism are unconstrained or unknown. The goal of this
 32 dissertation is to expand our knowledge of the wave-particle scattering mechanism
 33 that scatters electron microbursts.

34 This chapter serves as an introduction to the fundamental physical concepts
 35 that are essential to understand wave-particle interactions in Earth's magnetosphere.
 36 We will review the motion of charged particles in electric and magnetic fields, how
 37 particles are organized in the magnetosphere, how particles are accelerated and lost in
 38 the magnetosphere, and review the current state of our understanding of microbursts.

39 Then the rest of this dissertation expands our knowledge of microbursts. In
 40 Chapter ?? (chapter numbers will be filled in the full dissertation) we will investigate
 41 and model the scattering mechanism responsible for microbursts observed inside the
 42 outer radiation belt, near the magnetic equator. Then in Chapters ?? and ?? we
 43 will investigate the microburst scattering mechanism indirectly by estimating the
 44 microburst footprint size in low Earth orbit and the magnetic equator (near where
 45 microburst electrons are believed to be scattered) and compare it to sizes of chorus
 46 waves estimated in prior literature.

47 Charged Particle Motion in Electric and Magnetic Fields

A charged particle trapped in the magnetosphere will experience three types of periodic motion in Earth's nearly dipolar magnetic field. The three motions are ultimately due to the Lorentz force that a particle of momentum \vec{p} , charge q , and

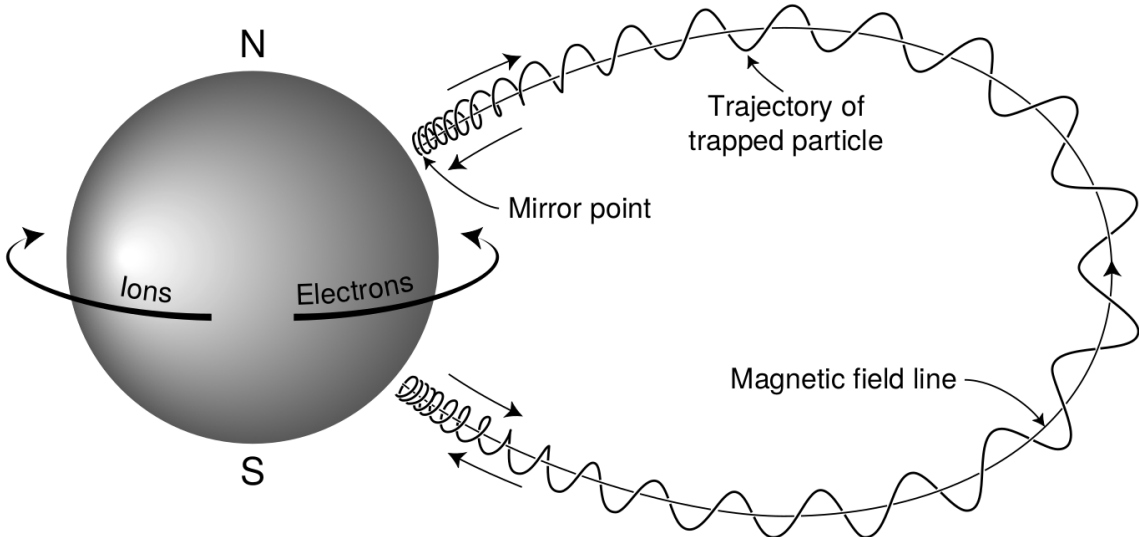


Figure 1.1: The three periodic motions of charged particles in Earth's dipole magnetic field. These motions are: gyration about the magnetic field line, bounce motion between the magnetic poles, and azimuthal drift around the Earth. Figure from (Baumjohann and Treumann, 1997).

velocity \vec{v} experiences in an electric field \vec{E} and magnetic field \vec{B} and is given by

$$\frac{d\vec{p}}{dt} = q(\vec{E} + \vec{v} \times \vec{B}). \quad (1.1)$$

- ⁴⁸ In the magnetosphere, the three periodic motions, in decreasing frequency, are
- ⁴⁹ gyration, bounce, and drift and are schematically shown in Fig. 1.1. Each periodic
- ⁵⁰ motion has a corresponding conserved quantity i.e. an adiabatic invariant.

The highest frequency periodic motion is gyration about a magnetic field of magnitude B . This motion is circular with a Larmor radius of

$$r = \frac{mv_{\perp}}{|q|B} \quad (1.2)$$

where m is the mass and v_{\perp} the particle's velocity perpendicular to \vec{B} . This motion

has a corresponding gyrofrequency

$$\Omega = \frac{|q|B}{m} \quad (1.3)$$

in units of radians/second. In the radiation belts, the electron gyrofrequency, Ω_e is on the order of a kHz. The corresponding adiabatic invariant is found by integrating the particle's canonical momentum around the particle's path of gyration

$$J_i = \oint (\vec{p} + q\vec{A}) \cdot d\vec{l} \quad (1.4)$$

where J_i is the i^{th} adiabatic invariant and \vec{A} is the magnetic vector potential. This integral is carried out by integrating the first term over the circumference of the gyro orbit and integrating the second term using Stokes theorem to calculate the magnetic flux enclosed by the gyro orbit. The gyration invariant is $J_1 \sim v_{\perp}^2/B$, which is conserved when the frequency, ω of a force acting on the gyrating electron satisfies

$$\omega \ll \Omega_e.$$

The second highest frequency periodic motion is bouncing due to a parallel gradient in \vec{B} . This periodic motion naturally arises in the magnetosphere because Earth's magnetic field is stronger near the poles, and artificially in the laboratory in magnetic bottle machines. To understand this motion we first we need to define the concept of pitch angle, α as the angle between \vec{B} and \vec{v} which is schematically shown in Fig. 1.2a. The pitch angle relates v with v_{\perp} , and v_{\parallel} (the component of the particles velocity parallel to \vec{B}). As shown in Fig. 1.2b and 1.2c, a smaller (larger) α will increase (decrease) the distance that the charged particle travels parallel to \vec{B} , during one gyration.

Assuming the particle's kinetic energy is conserved, the conservation of J_1 implies that given a particle's $v_{\perp}(0)$ and $B(0)$ at the magnetic equator (where

Earth's magnetic field is usually at a minimum), we can calculate its $v_{\perp}(s)$ along the particle's path s by calculating $B(s)$ from magnetic field models. Thus the particle's perpendicular velocity is then related via

$$\frac{v_{\perp}^2(0)}{B(0)} = \frac{v_{\perp}^2(s)}{B(s)} \quad (1.5)$$

⁶⁶ which can be rewritten as

$$\frac{v^2 \sin^2 \alpha(0)}{B(0)} = \frac{v^2 - v_{\parallel}^2(s)}{B(s)} \quad (1.6)$$

⁶⁷ and re-arranged to solve for $v_{\parallel}(s)$

$$v_{\parallel}(s) = v \sqrt{1 - \frac{B(s)}{B(0)} \sin^2 \alpha(0)} \quad (1.7)$$

⁶⁸ which will tend towards 0 when the second term in the radical approaches 1.

⁶⁹ The location where $v_{\parallel}(s) = 0$ is called the mirror point and is where a particle
⁷⁰ reverses direction. Since Earth's magnetic field is stronger towards the poles, the
⁷¹ mirroring particle will execute periodic bounce motion between its two mirror points
⁷² in the northern and southern hemispheres. The corresponding adiabatic invariant, J_2
⁷³ is

$$J_2 = \oint p_{\parallel} ds \quad (1.8)$$

where ds describes the particle path between the mirror points in the northern and southern hemispheres (see Fig. 1.1). J_2 is found by substituting Eq. 1.7 into Eq. 1.8 and defining the magnetic field strength at the mirror points as B_m (where $\alpha(m) =$

90°). The J_2 integral can be written as

$$J_2 = 2p \int_{m_n}^{m_s} \sqrt{1 - \frac{B(s)}{B(m)}} ds \quad (1.9)$$

74 where m_n and m_s are the northern and southern mirror points, respectively. The
 75 bounce period can be estimated (e.g. Baumjohann and Treumann, 1997) to be

$$t_b \approx \frac{LR_e}{\sqrt{W/m}} (3.7 - 1.6 \sin \alpha(0)) \quad (1.10)$$

76 where W is the particle's kinetic energy, and L is the L -shell. L -shell describes the
 77 distance from the Earth's center to the location where a particular magnetic field
 78 line crosses the magnetic equator, in units of Earth radii, R_e . As with gyration, the
 79 particle will bounce between the mirror points as long as $\omega \ll \Omega_b$, where Ω_b is the
 80 bounce frequency.

81 At this stage it is instructional to introduce the notion of the loss cone pitch
 82 angle, α_L . A particle with $\alpha \leq \alpha_L$ will mirror at or below ≈ 100 km altitude in
 83 the atmosphere. A charged particle gyrating at those altitudes will encounter and
 84 Coulomb scatter with the dense atmosphere and be lost from the magnetosphere.

85 The slowest periodic motion experienced by charged particles in Earth's mag-
 86 netic field is azimuthal drift around the Earth. This drift results from a combination of
 87 a radial gradient in \vec{B} and the curvature of the magnetic field. The radial gradient drift
 88 arises because Earth's magnetic field is stronger near the Earth where the particle's
 89 gyroradius radius of curvature shrinks as it gyrates towards stronger magnetic field,
 90 and expands when it gyrates outward. The overall effect is the particle gyro orbit does
 91 not close on itself and negatively charged particles drift east and positively charged
 92 particles drift west. The radial gradient drift is further enhanced by the centrifugal
 93 force that a particle experiences as it bounces along the curved field lines. The drift

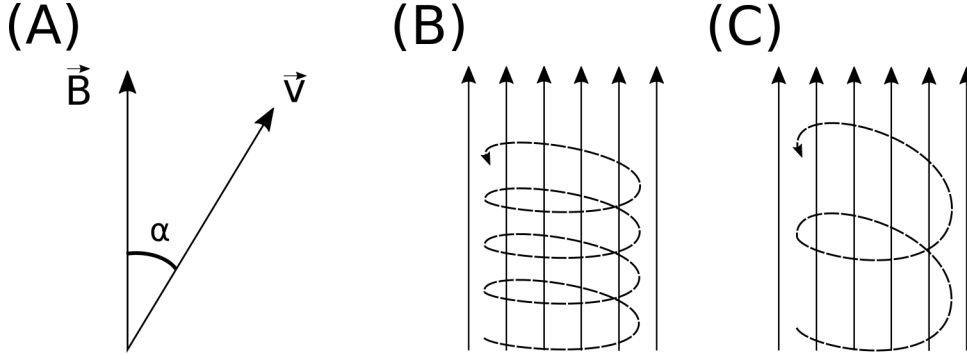


Figure 1.2: Charged particle motion in a uniform magnetic field \vec{B} . Panel (A) shows the geometry defining the pitch angle, α . Panel (B) and (C) show two helical electron trajectories with dashed lines assuming a large and small α (corresponding to a small and large parallel velocity $v_{||}$), respectively.

94 adiabatic invariant, J_3 is found by integrating Eq. 1.4 over the complete particle orbit
 95 around the Earth. The shape of this drift orbit is known as a drift shell. For J_3 , the
 96 first term is negligible and the second term is the magnetic flux enclosed by the drift
 97 shell, Φ_m i.e. $J_3 \sim \Phi_m$.

98 Figure 1.3 from Schulz and Lanzerotti (1974) shows contours of the gyration,
 99 bounce, and drift frequencies for electrons and protons in Earth's dipole magnetic
 100 field.

Up until now we have considered the three periodic motions due Earth's magnetic field in the absence of electric fields. If there is an electric field, E_{\perp} perpendicular to \vec{B} , a particle's center of gyration i.e., averaged position of the particle over a gyration, will drift with a velocity perpendicular to both E_{\perp} and \vec{B} . The drift velocity can be solved using Eq. 1.1 and is

$$\vec{v}_E = \frac{\vec{E} \times \vec{B}}{B^2}. \quad (1.11)$$

101 If there is a parallel magnetic field, $E_{||}$ then the particle is accelerated along the
 102 magnetic field line. An $E_{||}$ pointing away from the Earth will contribute to the mirror
 103 force and raise the particle's mirror point. On the contrary, an Earthward pointing

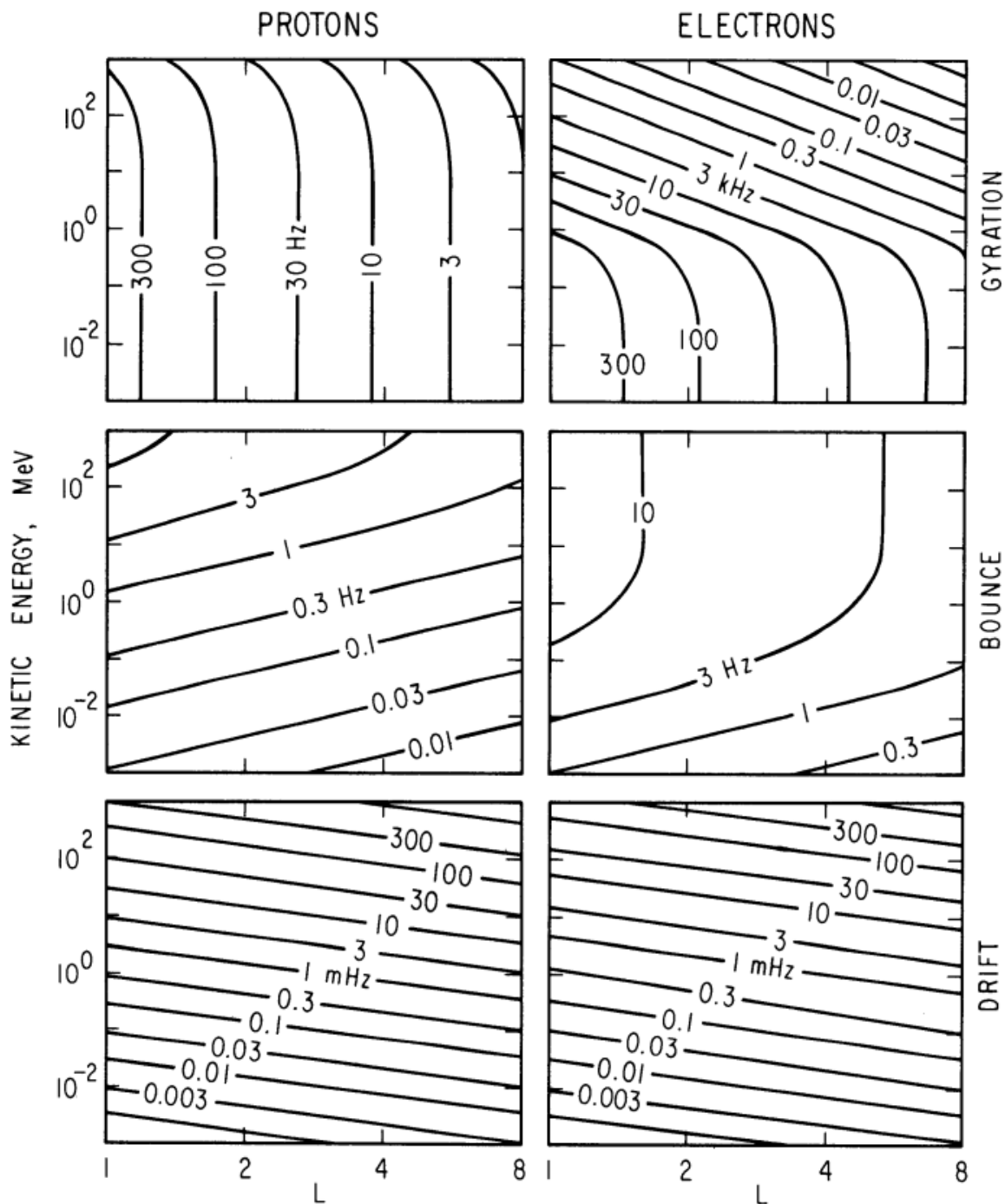


Figure 1.3: Contours of constant gyration, bounce, and drift frequencies for electrons and protons in a dipole field. Figure from Schulz and Lanzerotti (1974).

¹⁰⁴ $E_{||}$ will oppose the mirror force and lower the mirror point. If the Earthward $E_{||}$ is
¹⁰⁵ strong enough, the mirror point is lowered into the atmosphere that will precipitate
¹⁰⁶ particles. This is the mechanism that generates the aurora.

¹⁰⁷ Particle Populations and Their Interractions in the Magnetosphere

¹⁰⁸ Now that we have looked at the dynamics of single-particle motion in electric
¹⁰⁹ and magnetic fields, we will briefly tour the various macroscopic populations in the
¹¹⁰ magnetosphere that are illustrated in Fig. 1.4.

¹¹¹ The sun and its solar wind are ultimately the source of energy input into the
¹¹² magnetosphere. The solar wind at Earth's orbit is a plasma traveling at supersonic
¹¹³ speeds with an embedded interplanetary magnetic field (IMF). When the solar wind
¹¹⁴ encounters Earth's magnetic field, the plasma can not easily penetrate into the
¹¹⁵ magnetosphere because the plasma is frozen-in on magnetic field lines. Thus the
¹¹⁶ plasma and its magnetic field drapes around the magnetosphere, forming a cavity in
¹¹⁷ the solar wind that qualitatively has a shape as shown in Fig. 1.4. Because the solar
¹¹⁸ wind is supersonic at 1 AU, a bow shock exists upstream of the magnetosphere.
¹¹⁹ The solar wind plasma, after it is shocked by the bow shock, flows around the
¹²⁰ magnetosphere inside the magnetosheath. The surface where the solar wind ram
¹²¹ pressure and Earth's magnetic pressure balance is termed the magnetopause, which
¹²² can be thought of as a boundary between the solar wind and Earth's magnetosphere.
¹²³ This is a slightly naive description of the magnetopause, but is nonetheless an
¹²⁴ instructive conceptual picture. The shocked plasma then flows past the Earth where
¹²⁵ it shapes the magnetotail. In the magnetotail the magnetopause exists where the solar
¹²⁶ wind magnetic pressure balances Earth's magnetic field pressure in the lobes. The
¹²⁷ magnetotail extends on the order of $100 R_E$ downstream of Earth, and the tailward
¹²⁸ stretching of magnetic field lines creates the plasma sheet which exists in the region

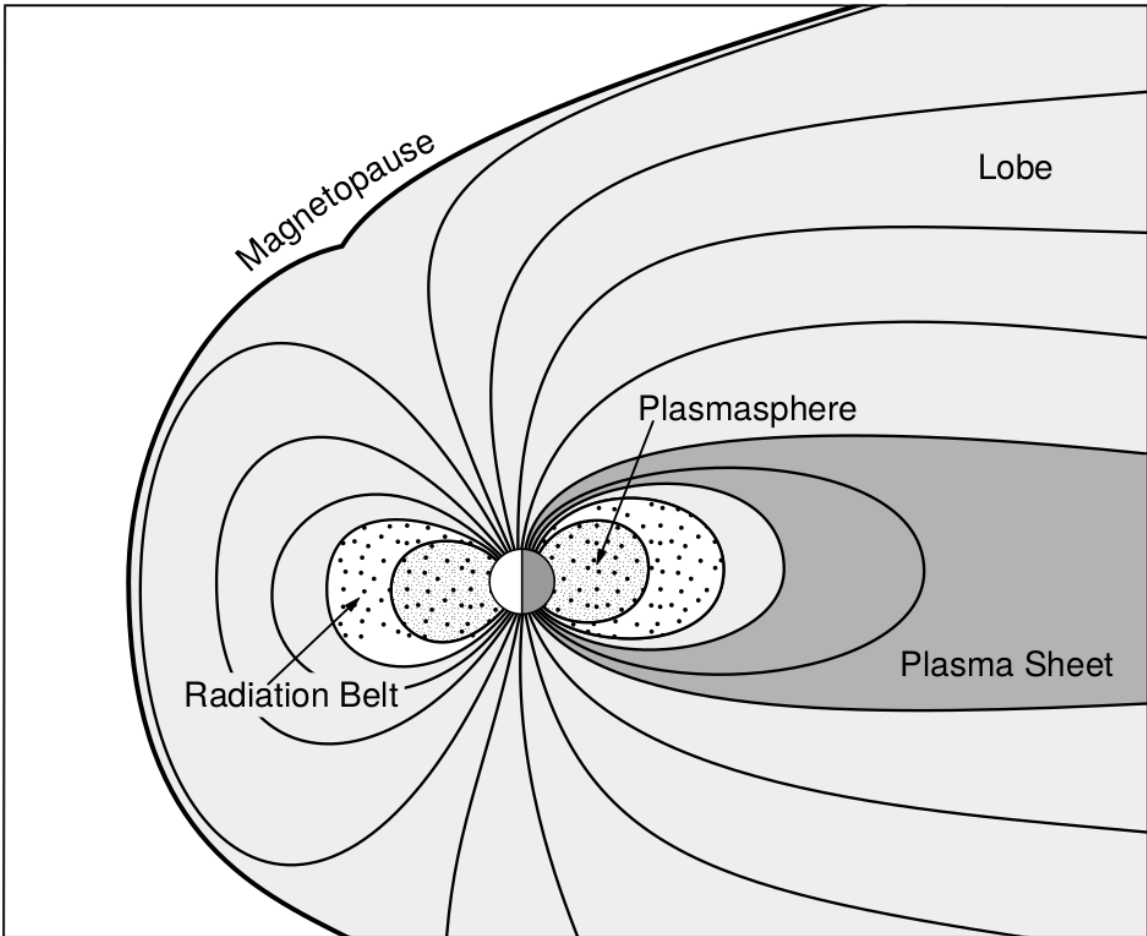


Figure 1.4: A few macroscopic structures in the magnetosphere. The magnetosphere boundary with the solar wind is the magnetopause. The magnetotail consists of two lobes that contain Earth's magnetic flux with the plasma sheet separating the two lobes. The inner magnetosphere contains the plasmasphere, the ring current, and the radiation belts which are co-located. Figure from Baumjohann and Treumann (1997).

¹²⁹ of low magnetic field strength near the magnetic equator (e.g. Eastwood et al., 2015).

¹³⁰ Populations in the Inner Magnetosphere

¹³¹ Closer to Earth, where the magnetic field is largely dipolar, are three plasma
¹³² populations that comprise the inner magnetosphere: the plasmasphere, the ring
¹³³ current, and the radiation belts which are shown in Fig. 1.4. Before we describe these
¹³⁴ three particle populations in detail, we will first introduce the coordinate system that
¹³⁵ most naturally describes the inner magnetosphere environment, and then the electric
¹³⁶ fields that effect mostly low energy particles.

¹³⁷ In this coordinate system the “radial” coordinate was defined in section 1 and
¹³⁸ is the L shell. The azimuthal coordinate is the magnetic local time (MLT). For an
¹³⁹ observer above Earth’s north pole looking down, MLT is defined to be 0 (midnight)
¹⁴⁰ in the anti-sunward direction, and increases in the counter-clockwise direction with 6
¹⁴¹ at dawn, 12 at noon (sunward direction), and 18 in dusk. The final coordinate is the
¹⁴² magnetic latitude, λ which is analogous to the latitude coordinate in the spherical
¹⁴³ coordinate system, and is defined to be 0 at the magnetic equator. This coordinate
¹⁴⁴ system is shown in Fig. 1.5 and naturally describes the inner magnetosphere
¹⁴⁵ populations described below.

¹⁴⁶ The low energy particle dynamics in the inner magnetosphere are organized by
¹⁴⁷ two electric fields: the co-rotation and the dawn-dusk electric fields. The co-rotation
¹⁴⁸ electric field arises from Earth’s rotation. The magnetic field and the particles frozen
¹⁴⁹ on it rotate with the Earth. To a non-rotating observer this rotation appears as a
¹⁵⁰ radial electric field that drops off as $\sim L^{-2}$. The other electric field, pointing from
¹⁵¹ dawn to dusk is called the convection electric field and is due to the Earthward
¹⁵² transport of particles from the magnetotail that appears as an electric field in Earth’s
¹⁵³ reference frame. The superposition of the co-rotation and convection electric

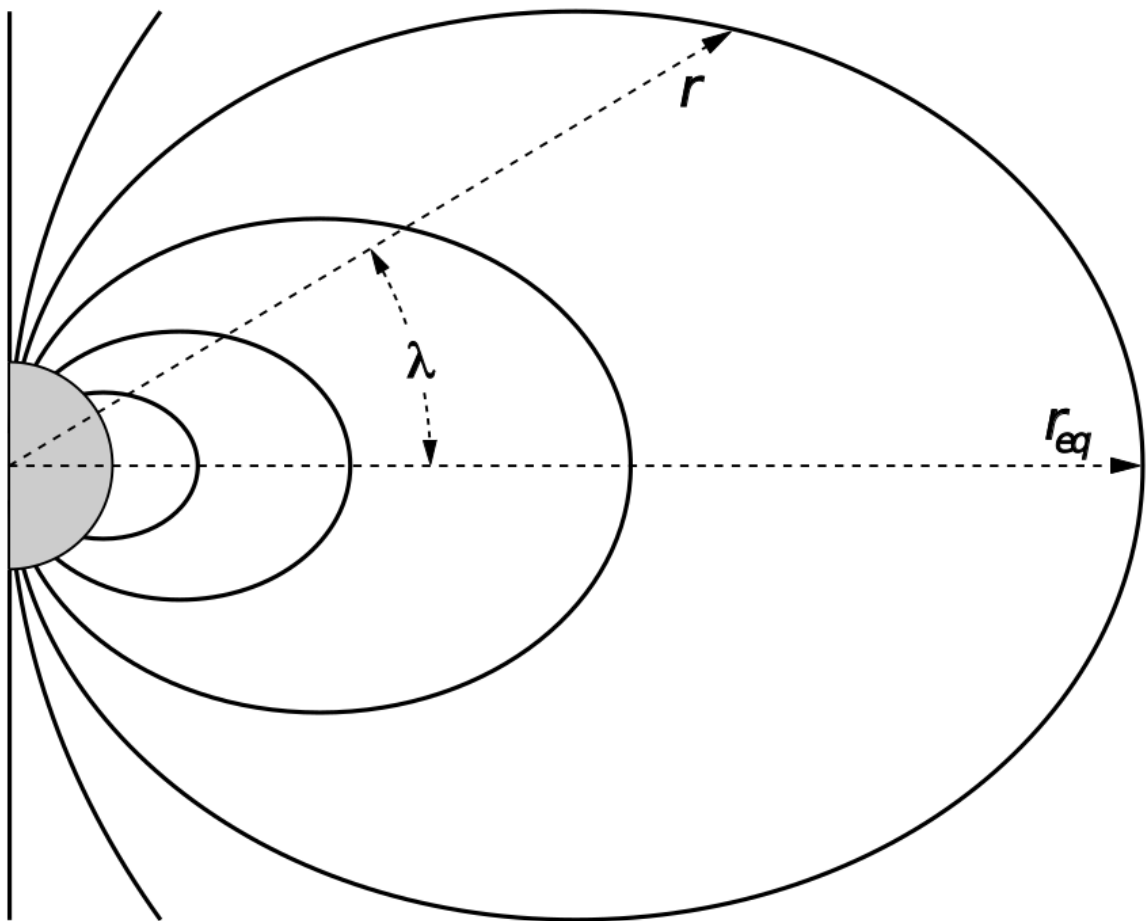


Figure 1.5: The dipole coordinate system. The magnetic latitude of \mathbf{r} is λ . The radial distance to a magnetic field line in the equatorial plane is typically given by $L = r_{eq}/R_e$. Figure from Baumjohann and Treumann (1997).

fields is a potential field shown in Fig. 1.6. The shaded area in Fig. 1.6 shows the orbits on which low energy electrons are trapped, and outside this region the particles are not trapped. The dynamic topology of the shaded region in Fig. 1.6 is controlled by only the convection electric field which is dependent on the solar wind speed and the IMF. The lowest energy particles that orbit in the shaded region in Fig. 1.6 make up the plasmasphere.

Plasmasphere The plasmasphere is a dense ($n_e \sim 10^3/\text{cm}^3$), cool ($\sim \text{eV}$) plasma. The plasmasphere typically extends to $L \sim 4$ and the spatial extent is highly dependent on the solar wind and magnetospheric conditions. The source of the plasmasphere is the ionosphere. The two main mechanisms that fill the plasmasphere with cold plasma are ionization of the ionosphere by sunlight and particle precipitation. The ultraviolet ionization by sunlight is strongly dependent on the time of day (day vs night), latitude (more ionization near the equator). The ionization due to particle precipitation, on the other hand, is highly dependent on magnetospheric conditions, and mostly occurs at high latitudes.

The outer boundary of the plasmasphere is the plasmapause which is typically identified as a steep radial gradient in plasma density from $\sim 10^3/\text{cm}^3$ to $\sim 1/\text{cm}^3$. The location of the plasmapause is important to model (e.g. O'Brien and Moldwin, 2003) and understand since the plasma density strongly controls the efficiency of particle scattering by waves (e.g. Horne et al., 2005).

Ring Current The next higher energy population is the ring current. This population consists of protons and electrons between tens and a few hundred keV that drift around the Earth. The orbits of higher energy particles are not as effected by the convection and co-rotation electric field, rather they drift around the Earth due to gradient and curvature drifts. Since the direction of the drift is dependent on

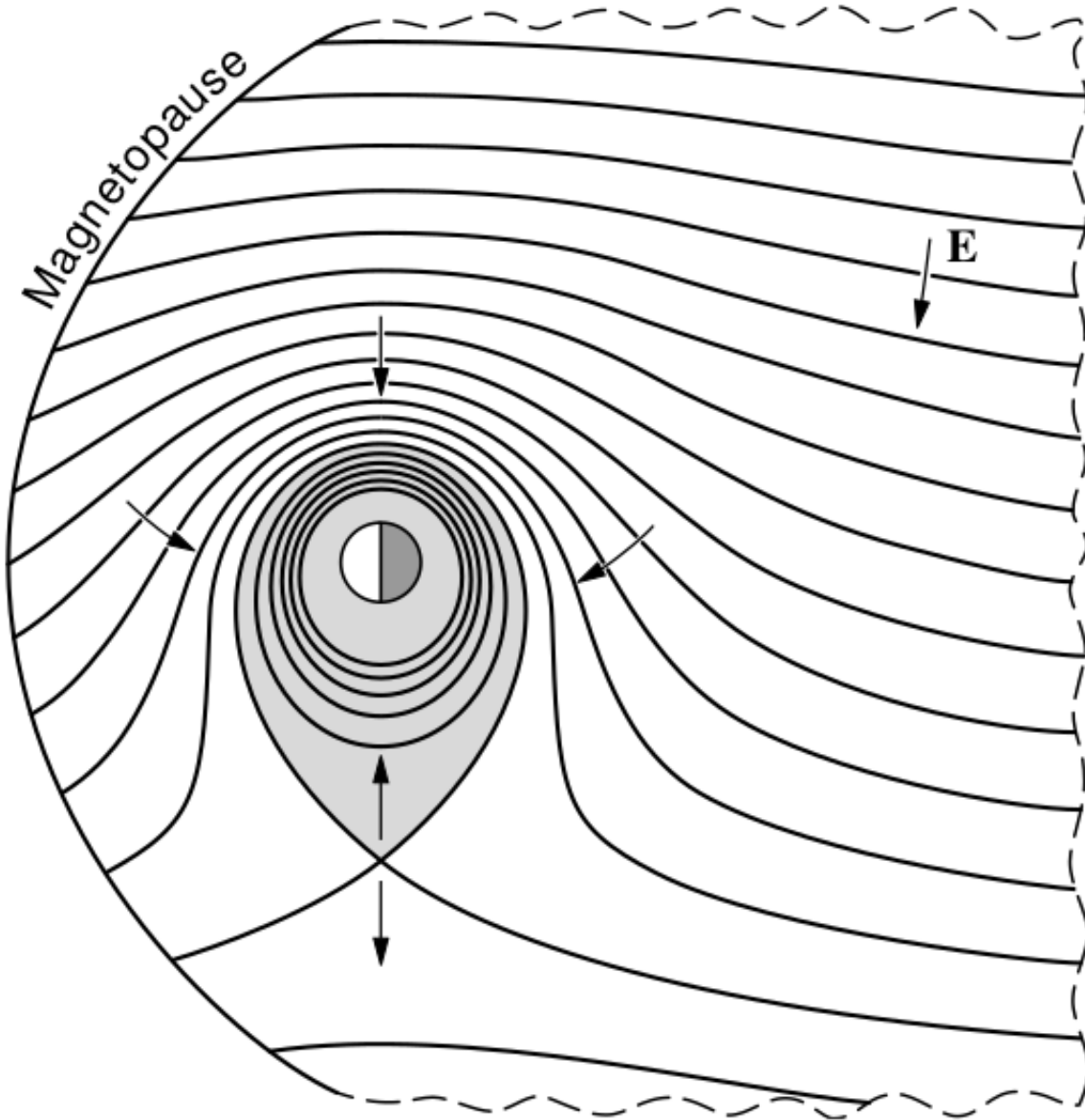


Figure 1.6: Equipotential lines and electric field arrows due to the superposition of the co-rotation and convection electric fields. Electrons in the shaded region execute closed orbits. Outside of the shaded regions the electrons are not trapped and will escape. The region separating the two regimes is called the Alfvén layer. Figure from Baumjohann and Treumann (1997).

¹⁷⁹ charge, protons drift west around the Earth and electrons drift East. This has the
¹⁸⁰ effect of creating a current around the Earth.

¹⁸¹ The ring current generates a magnetic field which decreases the magnetic field
¹⁸² strength at the surface of the Earth and increases it outside of the ring current.
¹⁸³ The decrease of Earth's magnetic field strength is readily observed by a system of
¹⁸⁴ ground-based magnetometers and is merged into a Disturbance Storm Time (DST)
¹⁸⁵ index to quantify the global reduction in the magnetic field. An example of a DST
¹⁸⁶ index time series from the 2015 St. Patrick's Day storm, driven by a coronal mass
¹⁸⁷ ejection (CME), is shown in Fig. 1.7. A few notable features of the storm and the
¹⁸⁸ ring current are worth pointing out. At the start of the storm the ring current is
¹⁸⁹ sometimes depleted and DST increases slightly (termed the initial phase or sudden
¹⁹⁰ storm commencement). Then the ring current population is rapidly built up and
¹⁹¹ DST rapidly decreases during the main phase. Lastly, after the storm passes, the
¹⁹² ring current gradually decays toward its equilibrium state over a period of a few
¹⁹³ days and DST returns towards 0 during the recovery phase. The DST index (along
¹⁹⁴ with other geomagnetic indices) are readily used by the space physics community to
¹⁹⁵ quantify the global state of the magnetosphere.

¹⁹⁶ Radiation Belts The highest particle energy populations are in the Van Allen
¹⁹⁷ radiation belts. These belts were discovered by Van Allen (1959) and Vernov and
¹⁹⁸ Chudakov (1960) during the Cold War and are a pair of toroidally shaped populations
¹⁹⁹ of trapped electrons and protons shown in Fig. 1.8. Their quiescent toroidal shape,
²⁰⁰ similar to the shape of the plasmasphere and ring current, is a result of Earth's dipole
²⁰¹ magnetic field.

²⁰² The inner radiation belt is extremely stable on time periods of years, extends
²⁰³ to $L \approx 2$, and mainly consists of protons with energies between MeV and GeV and

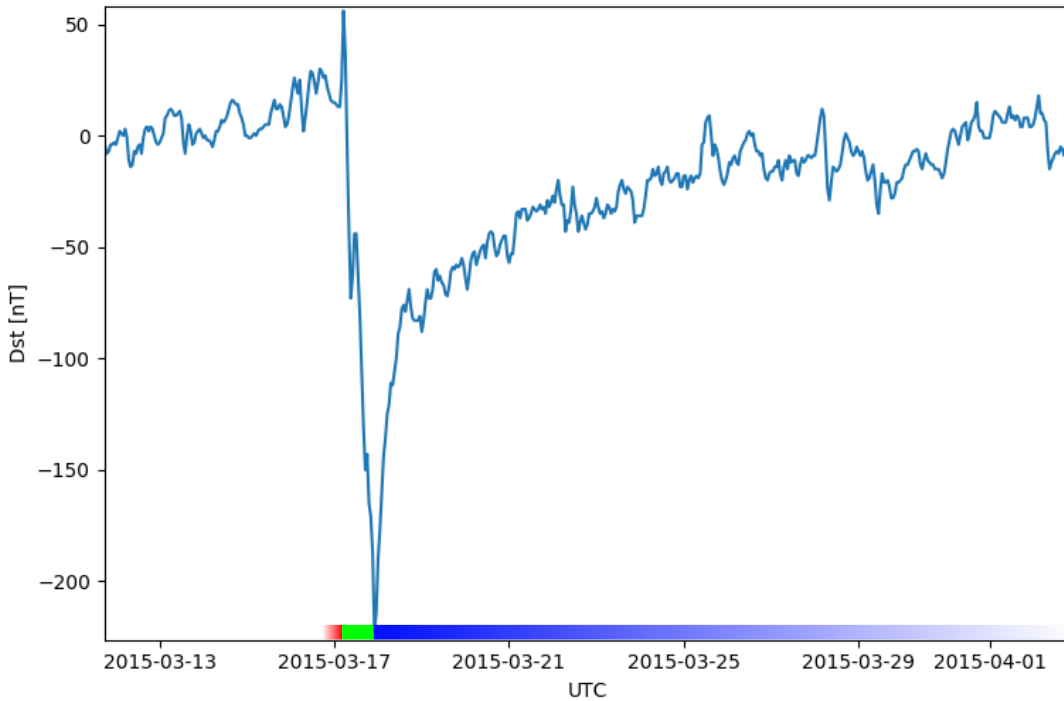


Figure 1.7: The DST index during the St. Patrick's Day 2015 storm. This storm was caused by a coronal mass ejection on March 15th, 2015. The storm phases are: initial phase, main phase, and recovery phase. The initial phase occurred when the Dst peaked at +50 nT on March 17th during which the ring current was eroded by the coronal mass ejection during the interval shown by the red bar shown at the bottom. Then the following rapid decrease to ≈ -200 nT was during the main phase where many injections from the magnetotail enhanced the ring current, which reduced Earth's magnetic field strength at the ground, and is shown with the green bar. Lastly, the recovery phase lasted from March 18th to approximately March 29th during which the ring current particles were lost and the ring current returned to its equilibrium state. The recovery phase is shown with the blue bar.

The Earth's Electron Radiation Belts

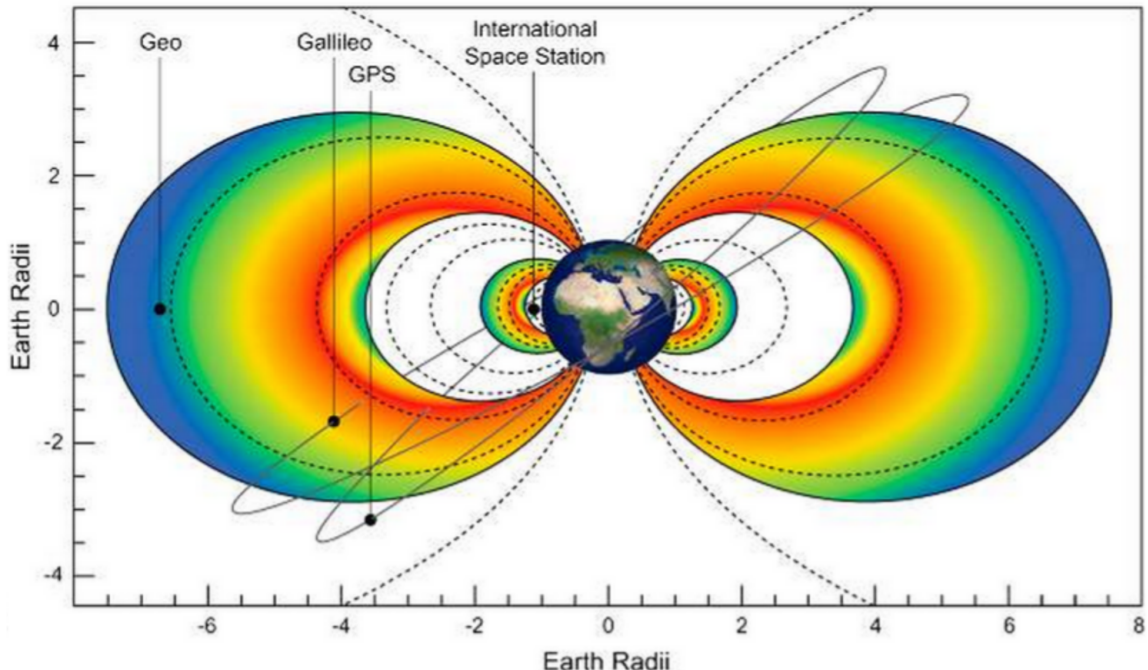


Figure 1.8: The two radiation belts with the locations of various satellites and orbits. Figure from (Horne et al., 2013).

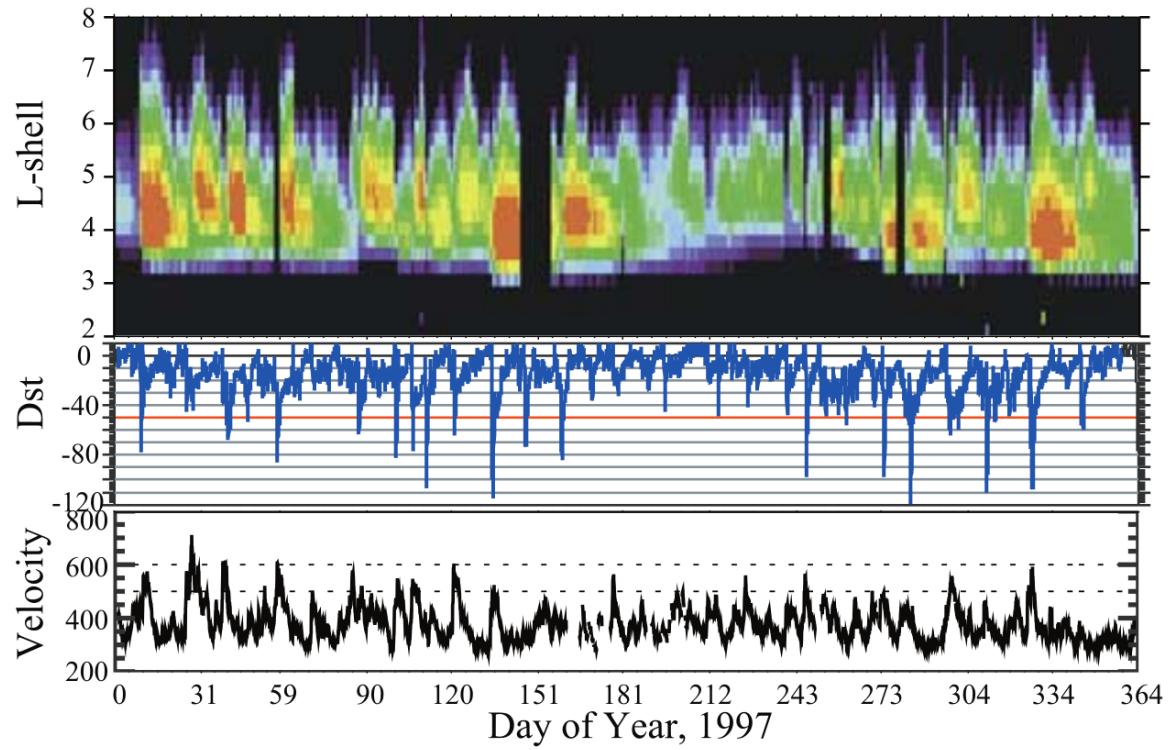


Figure 1.9: The dynamics of the outer radiation belt in 1997 from the POLAR satellite. Top panel shows the 1.2-2.4 MeV electron flux as a function of L and 1997 day of year. The middle panel shows the DST index, and bottom panel shows the solar wind velocity. Figure from (Reeves et al., 2003).

204 electrons with energies up to ≈ 1 MeV (Claudepierre et al., 2019). The source of
 205 inner radiation belt protons is believed to be due to cosmic-ray albedo neutron decay
 206 (e.g. Li et al., 2017) and inward radial diffusion for electrons (e.g. O'Brien et al.,
 207 2016). The gap between the inner and outer radiation belt is called the slot, which is
 208 believed to be due to hiss waves inside the plasmasphere (described below) scattering
 209 particles into the atmosphere (e.g. Breneman et al., 2015; Lyons and Thorne, 1973).

210 The outer radiation belt is much more dynamic and consists of mainly electrons
 211 of energies up to a few MeV. The outer belt's spatial extent is highly variable as
 212 shown in Fig. 1.9, and is typically observed between L of 4 and 8. The source of
 213 outer radiation belt electrons is widely believed to be injections of plasma from the
 214 magnetotail that is then accelerated to high energies.

215 Due to the highly energetic and dynamic nature of the radiation belts, and their
 216 impact on human presence in space, the radiation belts have been studied for over
 217 half century. Researchers have studied and attempted to predict the dynamics of
 218 radiation belt particles, waves, and wave-particle interactions by considering various
 219 competing particle acceleration and loss mechanisms which are described next.

220 Radiation Belt Particle Sources and Sinks

221 Adiabatic Heating

222 One of the particle heating and transport mechanisms arises from the Earthward
 223 convection of particles. The conservation of J_1 implies that the initial and final v_\perp
 224 depends on the change in the magnetic field amplitude

$$\frac{v_{\perp i}^2}{B_i} = \frac{v_{\perp f}^2}{B_f}. \quad (1.12)$$

²²⁵ As a particle convects Earthward, $B_f > B_i$ thus v_{\perp} must increase. The dipole
²²⁶ magnetic field amplitude can be written as

$$B(L, \theta) = \frac{31.2 \text{ } \mu\text{T}}{L^3} \sqrt{1 + 3 \cos^2 \theta}. \quad (1.13)$$

²²⁷ The change in v_{\perp}^2 can be found by taking the ratio of $B(L, \theta)$ at two different L shells

$$\frac{v_{\perp f}^2}{v_{\perp i}^2} = \left(\frac{L_i}{L_f} \right)^3 \quad (1.14)$$

²²⁸ thus the increase in $v_{\perp} \sim (L_i/L_f)^{3/2}$.

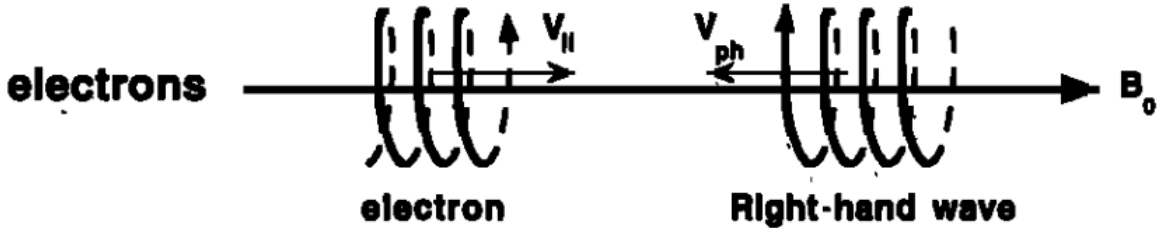
²²⁹ As the particle convects Earthward its v_{\parallel} also increases because the distance
²³⁰ between the particle's mirror points decrease. If J_2 is conserved, the shrinking bounce
²³¹ path implies that v_{\parallel} must increase by

$$\frac{v_{\parallel f}^2}{v_{\parallel i}^2} = \left(\frac{L_i}{L_f} \right)^k \quad (1.15)$$

²³² where k ranges from 2 for equatorial pitch angles, $\alpha_{eq} = 0^\circ$, to 2.5 for $\alpha_{eq} = 90^\circ$
²³³ (Baumjohann and Treumann, 1997). Since the rate of adiabatic heating is greater in
²³⁴ the perpendicular direction than heating in the parallel direction, an initially isotropic
²³⁵ particle distribution will become anisotropic during its convection. These isotropic
²³⁶ particles can then become unstable to wave growth and generate waves in order to
²³⁷ reach equilibrium.

²³⁸ Wave Resonance Heating

²³⁹ Another mechanism that heats particles is due to particles resonating with
²⁴⁰ plasma waves. A few of the electromagnetic wave modes responsible for particle
²⁴¹ acceleration (and scattering) relevant to radiation belt dynamics are hiss, whistler
²⁴² mode chorus (chorus), and electromagnetic ion cyclotron (EMIC) waves. These waves



$$\omega + k_{\parallel} v_{\parallel} = \Omega^-$$

Figure 1.10: The trajectories of an electron and a right-hand circularly polarized wave during a cyclotron resonance. The electron's v_{\parallel} and the wave's k_{\parallel} are in opposite directions such that the wave's frequency is Doppler shifted to an integer multiple of the electron cyclotron frequency. Figure from (Tsurutani and Lakhina, 1997).

243 are created by the loss cone instability that is driven by an anisotropy of electrons for
 244 chorus waves, and protons for EMIC waves. The level of anisotropy can be quantified
 245 by the ratio of the perpendicular to parallel particle temperatures (T_{\perp}/T_{\parallel}). A particle
 246 distribution is unstable when $T_{\perp}/T_{\parallel} > 1$. Since electrons gyrate in a right-handed
 247 sense, the chorus waves also tend to be right hand circularly polarized (Tsurutani and
 248 Lakhina, 1997). The same argument also applies to protons and left hand circularly
 249 polarized EMIC waves.

250 These circularly polarized waves can resonate with electrons and/or protons
 251 when their relative motion results in a static \vec{E} . One example of a resonance between
 252 a right hand circularly polarized wave and an electron is shown in Fig. 1.10. The
 253 electron's v_{\parallel} and the wave's parallel wave vector, k_{\parallel} are in opposite directions such
 254 that the wave frequency ω is Doppler shifted to an integer multiple of the Ω_e where the
 255 electron feels a static electric field and is accelerated or decelerated. Quantitatively,
 256 this resonance condition is easier to understand with the following toy model.

257 Assume a uniform magnetic field $\vec{B} = B_0 \hat{z}$ with a parallel propagating ($k = k \hat{z}$),
 258 right-hand circularly polarized wave. The wave's electric field as a function of position

²⁵⁹ and time can be written as

$$\vec{E} = E_0(\cos(\omega t - kz)\hat{x} + \sin(\omega t - kz)\hat{y}). \quad (1.16)$$

The angular component of \vec{E} that will effect the particle's v_{\perp} is

$$E_{\theta} = \vec{E} \cdot \hat{\theta} = E_0 \cos(\omega t - kz + \theta). \quad (1.17)$$

²⁶⁰ Now assume that the electron is traveling in the $-\hat{z}$ direction with a velocity $\vec{v} = -v_0\hat{z}$
²⁶¹ so its time dependent position along \hat{z} is

$$z(t) = -v_0t \quad (1.18)$$

²⁶² and gyrophase is

$$\theta(t) = -\Omega t + \theta(0) \quad (1.19)$$

²⁶³ where the first negative sign comes from the electron's negative charge. Now we put
²⁶⁴ this all together and find the force that the electron will experience

$$m \frac{dv_{\theta}}{dt} = qE_{\theta} = qE_0 \sin((\omega + kv_0 - \Omega)t + \theta(0)). \quad (1.20)$$

²⁶⁵ This is a relatively complex expression, but when the time dependent component is
²⁶⁶ 0, i.e.

$$\omega + kv_0 - \Omega = 0, \quad (1.21)$$

²⁶⁷ the electron will feel a static electric field and be accelerated or decelerated depending
²⁶⁸ on θ_0 , the phase between the wave and the electron. The expression in Eq. 1.21 is

²⁶⁹ commonly referred to as the resonance condition and is more generally written as

$$\omega - k_{||}v_{||} = \frac{n\Omega_e}{\gamma} \quad (1.22)$$

²⁷⁰ where n is the resonance order, and γ is the relativistic correction (e.g. Millan and
²⁷¹ Thorne, 2007). In the case of the cyclotron resonance, $\omega \approx \Omega_e$ thus J_1 is violated.
²⁷² Since J_1 is violated, J_2 and J_3 are also violated since the conditions required to violate
²⁷³ J_2 and J_3 are less stringent than J_1 . It is important to remember that a particle will
²⁷⁴ experience the effects of many waves along its drift orbit. The typical MLT extent
²⁷⁵ of a handful of waves that are capable of resonating with radiation belt electrons are
²⁷⁶ shown in Fig. 1.11.

²⁷⁷ Particle Losses

²⁷⁸ Now that we have seen two general mechanisms with which particles are
²⁷⁹ accelerated in the magnetosphere, we will now consider a few specific mechanisms
²⁸⁰ that remove particles from the magnetosphere into the atmosphere or the solar
²⁸¹ wind. One mechanism that transports magnetosperic particles into the solar wind
²⁸² is magnetopause shadowing (e.g. Ukhorskiy et al., 2006). Magnetopause shadowing
²⁸³ occurs when the ring current is strengthened and Earth's magnetic field strength is
²⁸⁴ increased outside of the ring current. If the ring current increases slowly enough (such
²⁸⁵ that J_3 is conserved), a particle drift shell will move outward to conserve J_3 . If the
²⁸⁶ particle's drift shell expands past the magnetopause, the particle will be lost to the
²⁸⁷ solar wind.

²⁸⁸ **Make sure I understand ULF waves and radial diffusion right** Another particle
²⁸⁹ loss (and acceleration) mechanism is driven by ultra low frequency (ULF) waves and
²⁹⁰ is called radial diffusion. Radial diffusion is the transport of particles from high
²⁹¹ to low phase space density, f . If the transport is radially inward, particles will

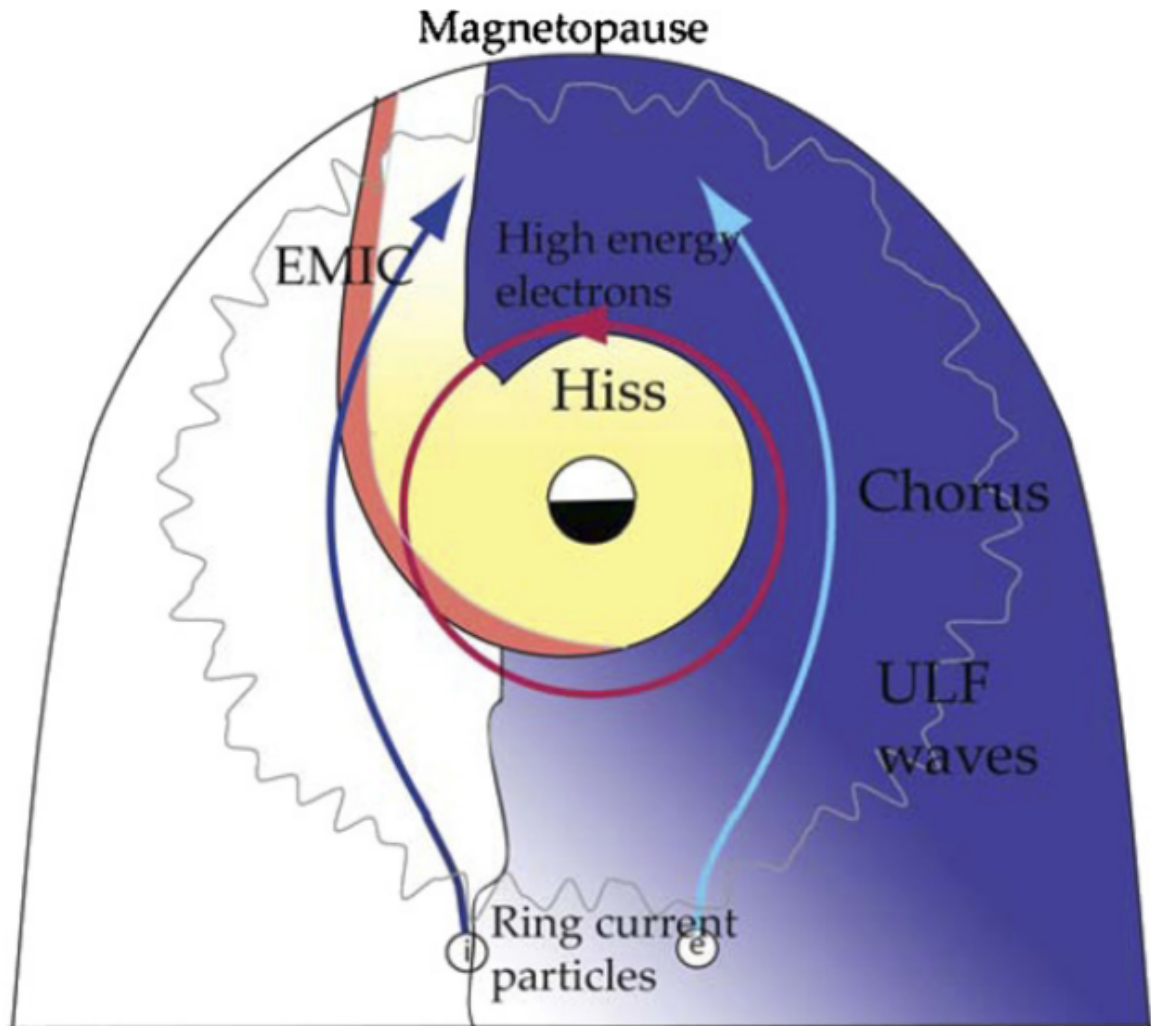


Figure 1.11: Various wave modes in the magnetosphere. Ultra low frequency waves occur through the magnetosphere. Chorus waves are typically observed in the 0-12 midnight-dawn region. EMIC waves are typically observed in the dusk MLT sector. Hiss waves are observed inside the plasmasphere. Figure from Millan and Thorne (2007).

292 appear to be accelerated. On the other hand, radially outward radial diffusion can
 293 transport particles through the magnetopause where they will be lost to the solar
 294 wind. Reeves et al. (2013) investigated the driver of particle acceleration during the
 295 October 2012 storm and observationally found that inward radial diffusion was not
 296 dominant, rather local acceleration via wave-resonance heating appeared to be the
 297 dominant acceleration mechanism.

298 The loss mechanism central to this dissertation is pitch angle and energy
 299 scattering of electrons by waves. Some of the waves that scatter electrons in energy
 300 and pitch angle in the inner magnetosphere are: plasmaspheric hiss (e.g. Breneman
 301 et al., 2015; O'Brien et al., 2014), EMIC waves (e.g. Capannolo et al., 2019; Hendry
 302 et al., 2017), and chorus waves (e.g. Breneman et al., 2017; Kasahara et al., 2018;
 303 Ozaki et al., 2019). These wave-particle interactions occur when the resonance
 304 condition in Eq. 1.22 is satisfied and the particle's energy and α is modified by
 305 the wave. More details regarding the theory of pitch angle and energy diffusion is
 306 given in Chapter ???. If the wave changes α towards 0 and $\alpha < \alpha_L$, then the particle's
 307 mirror point dips below 100 km altitude where the particle can be lost from the
 308 magnetosphere. One manifestation of pitch angle scattering of particles into the loss
 309 cone are microbursts: a sub-second durtaison impulse of electrons.

310

Microbursts

311 Microbursts were first with high altitude balloons which measured bremsstrahlung
 312 X-rays emitted by microburst electrons impacting the atmosphere by Anderson
 313 and Milton (1964). In the following years, numerous balloon flights expanded our
 314 knowledge of non-relativistic ($\lesssim 500$ keV) microbursts (relativistic microbursts have
 315 not yet been observed by high altitude balloons) by quantifying the microburst spatial
 316 extent, temporal width, occurrence frequency, extent in L and MLT, and their source.

317 The microburst source was first believed to be either a local plasma instability or a
 318 propagating disturbance in the magnetosphere (Barcus et al., 1966; Brown et al., 1965;
 319 Parks, 1967; Trefall et al., 1966). Soon after, both non-relativistic and relativistic
 320 microbursts electrons were directly observed in LEO with spacecraft including the
 321 Solar Anomalous and Magnetospheric Particle Explorer (SAMPEX) (e.g. Blake et al.,
 322 1996; Blum et al., 2015; Douma et al., 2019, 2017; Greeley et al., 2019; Lorentzen et al.,
 323 2001a,b; Nakamura et al., 1995, 2000; O'Brien et al., 2004, 2003), Montana State
 324 University's (MSU) Focused Investigation of Relativistic Electron Bursts: Intensity,
 325 Range, and Dynamics II (FIREBIRD-II) (Anderson et al., 2017; Breneman et al.,
 326 2017; Crew et al., 2016; Klumpar et al., 2015; Spence et al., 2012), and Science
 327 Technologies Satellite (STSAT-I) (e.g. Lee et al., 2012, 2005). An example microburst
 328 time series is shown in Fig. 1.12 and was observed by the FIREBIRD-II CubeSats.
 329 The prominent features of the example microbursts in Fig. 1.12 are their sub-second
 330 duration, half order of magnitude increase in count rate above the falling background,
 331 and their 200-800 keV energy extent.

332 Microbursts are observed on magnetic field footprints that are connected to the
 333 outer radiation belt (approximately $4 < L < 8$). They are predominately observed in
 334 the 0-12 MLT sector with an elevated occurrence frequency during magnetospherically
 335 disturbed times as shown in Fig. 1.13 (e.g. Douma et al., 2017). O'Brien et al. (2003)
 336 used SAMPEX relativistic electron data and found that microbursts predominately
 337 occur during the main phase of storms, with a heightened occurrence rate during the
 338 recovery phase. Microburst occurrence rates are also higher during high solar wind
 339 velocity events e.g. from co-rotating interaction regions (Greeley et al., 2019; O'Brien
 340 et al., 2003).

341 The estimated impact of microbursts on the atmosphere and the radiation
 342 belts is significant. Relativistic microburst electrons impacting the atmosphere are

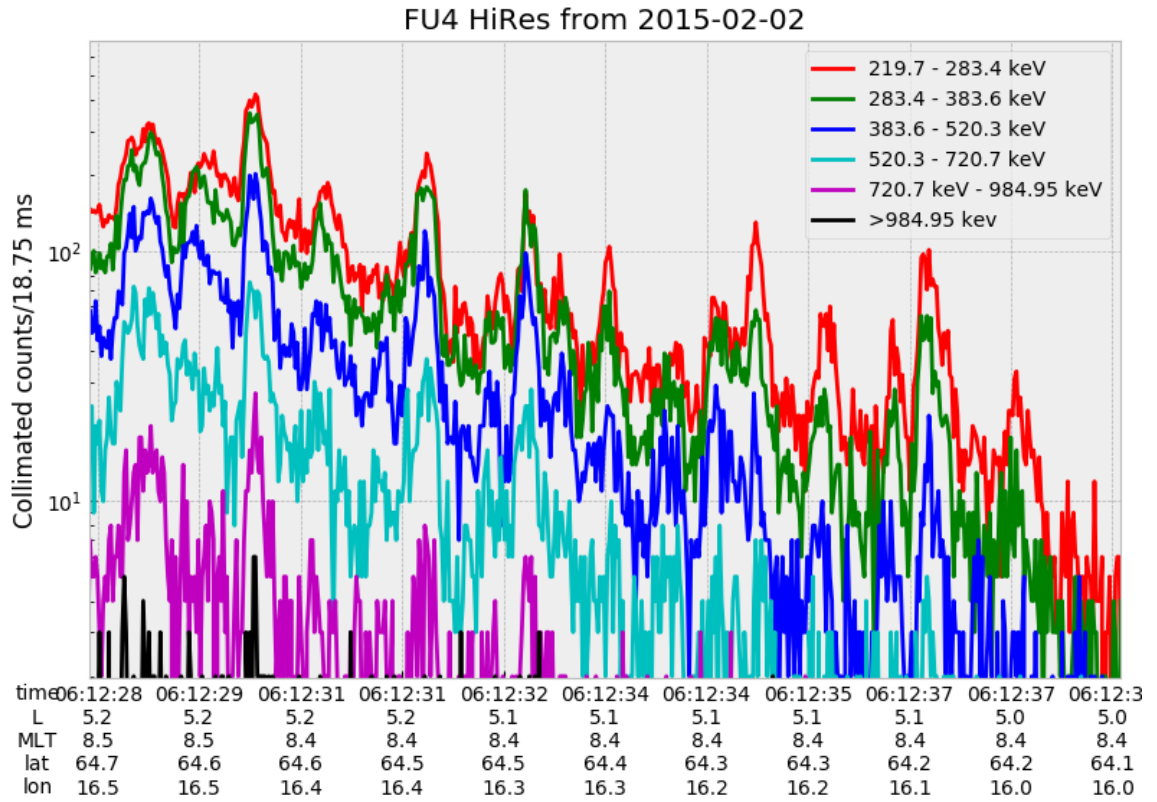


Figure 1.12: An example train of microbursts observed by FIREBIRD-II unit 4 on February 2nd, 2015. The colored curves show the differential energy channel count rates in five channels from ≈ 200 keV to 1 MeV and a sixth integral energy channel with a 1 MeV threshold. The x-axis labels show auxiliary information such as time of observation and the spacecraft position in L, MLT, latitude and longitude coordinates.

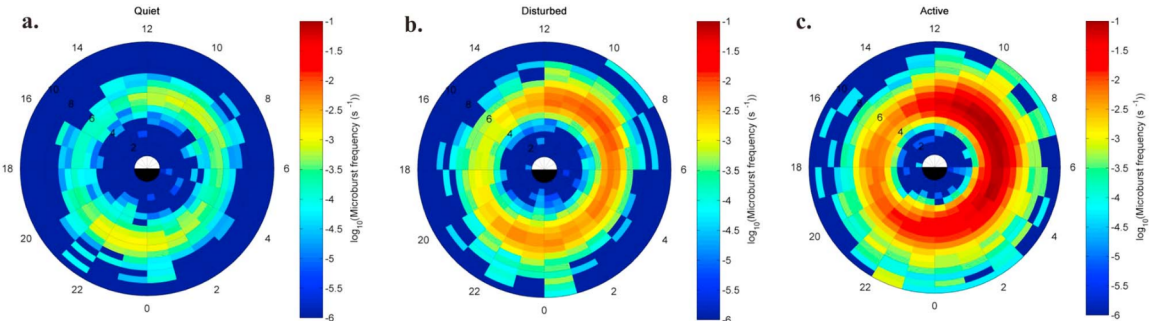


Figure 1.13: Distribution of > 1 MeV microburst occurrence rates as a function of L and MLT. The three panels show the microburst occurrence rate dependence on geomagnetic activity, parameterized by the auroral electrojet (AE) index for (a) $AE < 100$ nT, (b) $100 < AE < 300$ nT and (c) $AE > 300$ nT. Figure from Douma et al. (2017).

343 ionized at < 100 km altitudes, with higher energy electrons penetrating closer to
 344 the surface. The resulting chemical reaction of microburst electrons impacting the
 345 atmosphere produces odd hydrogen HO_x and odd nitrogen NO_x molecules, which
 346 are partially responsible for destroying ozone (O_3). Seppälä et al. (2018) modeled
 347 a six hour relativistic microburst storm and found that the mesospheric ozone was
 348 reduced by 7 – 12% in the summer months and 12 – 20% in the winter months, so
 349 microbursts may have a non-negligible contribution to the dynamics of atmospheric
 350 ozone. Furthermore, microbursts have also been estimated to have a significant
 351 impact on the outer radiation belt electron population. Radiation belt electron loss
 352 due to microbursts has been estimated to be on the order of a day (Breneman
 353 et al., 2017; Douma et al., 2019; Lorentzen et al., 2001b; O'Brien et al., 2004; Thorne
 354 et al., 2005).

355 The wave-particle interactions responsible for generating microbursts are also
 356 believed to accelerate electrons in the radiation belts. As mentioned earlier, when
 357 an electron is in resonance with a wave, energy is exchanged with the wave and
 358 the electron is either accelerated or decelerated. The signature of wave-particle

359 acceleration been observed for radiation belt electrons (e.g. Horne et al., 2005;
 360 Meredith et al., 2002; Reeves et al., 2013), and O'Brien et al. (2003) presented evidence
 361 that enhancements in chorus waves, microbursts, and radiation belt electrons are
 362 related. To explain their observations, O'Brien et al. (2003) proposed that microburst
 363 precipitation is a side effect of electron acceleration due to chorus waves.

364 The widely used theoretical framework to model the wave-particle interactions
 365 responsible for accelerating electrons and scattering microbursts is quasi-linear
 366 diffusion (e.g. Horne et al., 2005; Meredith et al., 2002; Summers, 2005; Summers
 367 et al., 1998; Thorne et al., 2005; Walker, 1993). This framework is explained in
 368 Chapter ??, and applied to an observation of a microburst in the heart of the
 369 radiation belt. Qualitatively, when a particle is resonant with a wave it can either
 370 be transported in pitch angle towards the loss cone and lose energy to the wave, or
 371 transported away from the loss cone and gain energy from the wave.

372 As previously mentioned, the range of observed microburst energies range from a
 373 few tens of keV (e.g Datta et al., 1997; Parks, 1967) to greater than 1 MeV (e.g. Blake
 374 et al., 1996; Greeley et al., 2019). The microburst electron flux (J) falls off in energy,
 375 and the microburst energy spectra is typically well fit to a decaying exponential

$$J(E) = J_0 e^{-E/E_0} \quad (1.23)$$

376 where J_0 is the flux at 0 keV (unphysical free parameter) and E_0 quantifies the
 377 efficiency of the scattering mechanism in energy (e.g. Datta et al., 1997; Lee et al.,
 378 2005; Parks, 1967). A small E_0 suggests that mostly low energy particles are scattered.
 379 In contrast a high E_0 suggests that the scattering mechanism scatters low and high
 380 energy electrons. Reality is a bit more messy and a high E_0 may be a signature of
 381 a scattering mechanism preferential to high energy electrons, but is hidden by the

382 convolution of the source particles available to be scattered (typically with a falling
 383 energy spectrum) and the energy-dependent efficiency of the scattering mechanism.

384 The short microburst duration observed by a single LEO satellite has an
 385 ambiguity when interpreting what is exactly a microburst. The two possible realities
 386 are: a microburst is very small and spatially stationary so that the LEO spacecraft
 387 passes through it in less than a second. Alternatively, microbursts are spatially large
 388 and transient so a microburst will pass by the spacecraft in a fraction of a second.
 389 There are a few ways to distinguish between the two possible realities, and each one
 390 has a unique set of advantages.

391 A high altitude balloon provides essentially a stationary view of the precipitating
 392 particles under the radiation belt footprints. A short-lived, temporal microburst can
 393 be unambiguously identified. Spatial structures, on the other hand, are difficult to
 394 identify because a balloon is essentially still on drift timescales.

395 Multi-spacecraft missions are an alternate solution that can determine if a
 396 microburst is spatial or temporal. As will be shown in this dissertation, if a microburst
 397 is observed simultaneously by two spacecraft then it is temporal and has a size
 398 greater than the spacecraft separation. On the contrary, if two spacecraft observe
 399 a microburst-like feature at different times but at the same location, then the feature
 400 is spatial and may be a curtain (Blake and O'Brien, 2016). Both balloon and multi-
 401 spacecraft observational methods have a unique set of strengths, and this dissertation
 402 takes the multi-spacecraft approach to identify and study microbursts.

403 Scope of Reserach

404 This dissertation furthers our understanding of the microburst scattering
 405 mechanism by presenting observational evidence of microburst scattering directly, and
 406 measuring microburst sizes and comparing them to the size of chorus waves. Chapter

407 ?? describes a microburst scattering event observed by NASA’s Van Allen Probes.
408 For this event, particle and wave measurements were analyzed and modeled in the
409 theoretical framework of pitch angle and energy diffusion. Then the following two
410 chapters present studies of microburst sizes in comparison to chorus waves. Chapter
411 ?? describes a bouncing packet microburst observation made by the FIREBIRD-II
412 mission where the microburst’s lower bound longitudinal and latitudinal sizes were
413 estimated. Then Chapter ?? expands the case study from Chapter ?? to a statistical
414 study of microburst sizes using The Aerospace Corporation’s AeroCube-6 (AC6)
415 CubeSats. In this study, a Monte Carlo and analytic microburst size models were
416 developed to account for the compounding statistical effects of random microburst
417 sizes and locations. Lastly, Chapter ?? will summarize this work and make concluding
418 remarks regarding outstanding questions in microburst physics.

- 420 Anderson, B., Shekhar, S., Millan, R., Crew, A., Spence, H., Klumpar, D., Blake, J.,
421 O'Brien, T., and Turner, D. (2017). Spatial scale and duration of one microburst
422 region on 13 August 2015. *Journal of Geophysical Research: Space Physics*.

423 Anderson, K. A. and Milton, D. W. (1964). Balloon observations of X rays in the
424 auroral zone: 3. High time resolution studies. *Journal of Geophysical Research*, 69(21):4457–4479.

425 Barcus, J., Brown, R., and Rosenberg, T. (1966). Spatial and temporal character of
426 fast variations in auroral-zone x rays. *Journal of Geophysical Research*, 71(1):125–
427 141.

428 Baumjohann, W. and Treumann, R. A. (1997). *Basic space plasma physics*. World
429 Scientific.

430 Blake, J.,Looper, M., Baker, D., Nakamura, R., Klecker, B., and Hovestadt, D.
431 (1996). New high temporal and spatial resolution measurements by sampex of the
432 precipitation of relativistic electrons. *Advances in Space Research*, 18(8):171 – 186.

433 Blake, J. B. and O'Brien, T. P. (2016). Observations of small-scale latitudinal
434 structure in energetic electron precipitation. *Journal of Geophysical Research: Space Physics*, 121(4):3031–3035. 2015JA021815.

435 Blum, L., Li, X., and Denton, M. (2015). Rapid MeV electron precipitation as
436 observed by SAMPEX/HILT during high-speed stream-driven storms. *Journal of
437 Geophysical Research: Space Physics*, 120(5):3783–3794. 2014JA020633.

438 Breneman, A., Crew, A., Sample, J., Klumpar, D., Johnson, A., Agapitov, O.,
439 Shumko, M., Turner, D., Santolik, O., Wygant, J., et al. (2017). Observations
440 directly linking relativistic electron microbursts to whistler mode chorus: Van allen
441 probes and FIREBIRD II. *Geophysical Research Letters*.

442 Breneman, A. W., Halford, A., Millan, R., McCarthy, M., Fennell, J., Sample, J.,
443 Woodger, L., Hospodarsky, G., Wygant, J. R., Cattell, C. A., et al. (2015). Global-
444 scale coherence modulation of radiation-belt electron loss from plasmaspheric hiss.
445 *Nature*, 523(7559):193.

446 Brown, R., Barcus, J., and Parsons, N. (1965). Balloon observations of auroral zone
447 x rays in conjugate regions. 2. microbursts and pulsations. *Journal of Geophysical
448 Research (U.S.)*.

449 Capannolo, L., Li, W., Ma, Q., Shen, X.-C., Zhang, X.-J., Redmon, R., Rodriguez,
450 J., Engebretson, M., Kletzing, C., Kurth, W., et al. (2019). Energetic electron
451 precipitation: multi-event analysis of its spatial extent during emic wave activity.
452 *Journal of Geophysical Research: Space Physics*.

453

- 455 Claudepierre, S., O'Brien, T.,Looper, M., Blake, J., Fennell, J., Roeder, J.,
 456 Clemmons, J., Mazur, J., Turner, D., Reeves, G., et al. (2019). A revised look
 457 at relativistic electrons in the earth's inner radiation zone and slot region. *Journal*
 458 *of Geophysical Research: Space Physics*, 124(2):934–951.
- 459 Crew, A. B., Spence, H. E., Blake, J. B., Klumpar, D. M., Larsen, B. A., O'Brien,
 460 T. P., Driscoll, S., Handley, M., Legere, J., Longworth, S., Mashburn, K.,
 461 Mosleh, E., Ryhajlo, N., Smith, S., Springer, L., and Widholm, M. (2016). First
 462 multipoint in situ observations of electron microbursts: Initial results from the
 463 NSF FIREBIRD II mission. *Journal of Geophysical Research: Space Physics*,
 464 121(6):5272–5283. 2016JA022485.
- 465 Datta, S., Skoug, R., McCarthy, M., and Parks, G. (1997). Modeling of microburst
 466 electron precipitation using pitch angle diffusion theory. *Journal of Geophysical*
 467 *Research: Space Physics*, 102(A8):17325–17333.
- 468 Douma, E., Rodger, C., Blum, L., O'Brien, T., Clilverd, M., and Blake, J. (2019).
 469 Characteristics of relativistic microburst intensity from sampex observations.
 470 *Journal of Geophysical Research: Space Physics*.
- 471 Douma, E., Rodger, C. J., Blum, L. W., and Clilverd, M. A. (2017). Occurrence
 472 characteristics of relativistic electron microbursts from SAMPEX observations.
 473 *Journal of Geophysical Research: Space Physics*, 122(8):8096–8107. 2017JA024067.
- 474 Eastwood, J., Hietala, H., Toth, G., Phan, T., and Fujimoto, M. (2015). What
 475 controls the structure and dynamics of earths magnetosphere? *Space Science*
 476 *Reviews*, 188(1-4):251–286.
- 477 Greeley, A., Kanekal, S., Baker, D., Klecker, B., and Schiller, Q. (2019). Quantifying
 478 the contribution of microbursts to global electron loss in the radiation belts. *Journal*
 479 *of Geophysical Research: Space Physics*.
- 480 Hendry, A. T., Rodger, C. J., and Clilverd, M. A. (2017). Evidence of sub-mev
 481 emic-driven electron precipitation. *Geophysical Research Letters*, 44(3):1210–1218.
- 482 Horne, R., Glauert, S., Meredith, N., Boscher, D., Maget, V., Heynderickx, D., and
 483 Pitchford, D. (2013). Space weather impacts on satellites and forecasting the earth's
 484 electron radiation belts with spacecast. *Space Weather*, 11(4):169–186.
- 485 Horne, R. B., Thorne, R. M., Shprits, Y. Y., Meredith, N. P., Glauert, S. A., Smith,
 486 A. J., Kanekal, S. G., Baker, D. N., Engebretson, M. J., Posch, J. L., et al.
 487 (2005). Wave acceleration of electrons in the van allen radiation belts. *Nature*,
 488 437(7056):227.
- 489 Kasahara, S., Miyoshi, Y., Yokota, S., Mitani, T., Kasahara, Y., Matsuda, S.,
 490 Kumamoto, A., Matsuoka, A., Kazama, Y., Frey, H., et al. (2018). Pulsating
 491 aurora from electron scattering by chorus waves. *Nature*, 554(7692):337.

- 492 Klumper, D., Springer, L., Mosleh, E., Mashburn, K., Berardinelli, S., Gunderson,
 493 A., Handly, M., Ryhajlo, N., Spence, H., Smith, S., Legere, J., Widholm, M.,
 494 Longworth, S., Crew, A., Larsen, B., Blake, J., and Walmsley, N. (2015). Flight
 495 system technologies enabling the twin-cubesat firebird-ii scientific mission.
- 496 Lee, J. J., Parks, G. K., Lee, E., Tsurutani, B. T., Hwang, J., Cho, K. S., Kim, K.-H.,
 497 Park, Y. D., Min, K. W., and McCarthy, M. P. (2012). Anisotropic pitch angle
 498 distribution of 100 keV microburst electrons in the loss cone: measurements from
 499 STSAT-1. *Annales Geophysicae*, 30(11):1567–1573.
- 500 Lee, J.-J., Parks, G. K., Min, K. W., Kim, H. J., Park, J., Hwang, J., McCarthy,
 501 M. P., Lee, E., Ryu, K. S., Lim, J. T., Sim, E. S., Lee, H. W., Kang, K. I., and
 502 Park, H. Y. (2005). Energy spectra of 170–360 keV electron microbursts measured
 503 by the korean STSAT-1. *Geophysical Research Letters*, 32(13). L13106.
- 504 Li, X., Selesnick, R., Schiller, Q., Zhang, K., Zhao, H., Baker, D. N., and Temerin,
 505 M. A. (2017). Measurement of electrons from albedo neutron decay and neutron
 506 density in near-earth space. *Nature*, 552(7685):382.
- 507 Lorentzen, K. R., Blake, J. B., Inan, U. S., and Bortnik, J. (2001a). Observations
 508 of relativistic electron microbursts in association with VLF chorus. *Journal of
 509 Geophysical Research: Space Physics*, 106(A4):6017–6027.
- 510 Lorentzen, K. R., Looper, M. D., and Blake, J. B. (2001b). Relativistic electron
 511 microbursts during the GEM storms. *Geophysical Research Letters*, 28(13):2573–
 512 2576.
- 513 Lyons, L. R. and Thorne, R. M. (1973). Equilibrium structure of radiation belt
 514 electrons. *Journal of Geophysical Research*, 78(13):2142–2149.
- 515 Meredith, N., Horne, R., Summers, D., Thorne, R., Iles, R., Heynderickx, D., and
 516 Anderson, R. (2002). Evidence for acceleration of outer zone electrons to relativistic
 517 energies by whistler mode chorus. In *Annales Geophysicae*, volume 20, pages 967–
 518 979.
- 519 Millan, R. and Thorne, R. (2007). Review of radiation belt relativistic electron losses.
 520 *Journal of Atmospheric and Solar-Terrestrial Physics*, 69(3):362 – 377.
- 521 Nakamura, R., Baker, D. N., Blake, J. B., Kanekal, S., Klecker, B., and Hovestadt,
 522 D. (1995). Relativistic electron precipitation enhancements near the outer edge of
 523 the radiation belt. *Geophysical Research Letters*, 22(9):1129–1132.
- 524 Nakamura, R., Isowa, M., Kamide, Y., Baker, D., Blake, J., and Looper, M. (2000).
 525 Observations of relativistic electron microbursts in association with VLF chorus.
 526 *J. Geophys. Res.*, 105:15875–15885.

- 527 O'Brien, T., Claudepierre, S., Blake, J., Fennell, J. F., Clemons, J., Roeder, J.,
 528 Spence, H. E., Reeves, G., and Baker, D. (2014). An empirically observed pitch-
 529 angle diffusion eigenmode in the earth's electron belt near $l^* = 5.0$. *Geophysical*
 530 *Research Letters*, 41(2):251–258.
- 531 O'Brien, T., Claudepierre, S., Guild, T., Fennell, J., Turner, D., Blake, J., Clemons,
 532 J., and Roeder, J. (2016). Inner zone and slot electron radial diffusion revisited.
 533 *Geophysical Research Letters*, 43(14):7301–7310.
- 534 O'Brien, T. and Moldwin, M. (2003). Empirical plasmapause models from magnetic
 535 indices. *Geophysical Research Letters*, 30(4).
- 536 O'Brien, T. P.,Looper, M. D., and Blake, J. B. (2004). Quantification of relativistic
 537 electron microburst losses during the GEM storms. *Geophysical Research Letters*,
 538 31(4). L04802.
- 539 O'Brien, T. P., Lorentzen, K. R., Mann, I. R., Meredith, N. P., Blake, J. B., Fennell,
 540 J. F., Looper, M. D., Milling, D. K., and Anderson, R. R. (2003). Energization of
 541 relativistic electrons in the presence of ULF power and MeV microbursts: Evidence
 542 for dual ULF and VLF acceleration. *Journal of Geophysical Research: Space*
 543 *Physics*, 108(A8).
- 544 Ozaki, M., Miyoshi, Y., Shiokawa, K., Hosokawa, K., Oyama, S.-i., Kataoka, R.,
 545 Ebihara, Y., Ogawa, Y., Kasahara, Y., Yagitani, S., et al. (2019). Visualization of
 546 rapid electron precipitation via chorus element wave–particle interactions. *Nature*
 547 *communications*, 10(1):257.
- 548 Parks, G. K. (1967). Spatial characteristics of auroral-zone X-ray microbursts. *Journal*
 549 *of Geophysical Research*, 72(1):215–226.
- 550 Reeves, G., Spence, H. E., Henderson, M., Morley, S., Friedel, R., Funsten, H., Baker,
 551 D., Kanekal, S., Blake, J., Fennell, J., et al. (2013). Electron acceleration in the
 552 heart of the van allen radiation belts. *Science*, 341(6149):991–994.
- 553 Reeves, G. D., McAdams, K. L., Friedel, R. H. W., and O'Brien, T. P. (2003). Ac-
 554 celeration and loss of relativistic electrons during geomagnetic storms. *Geophysical*
 555 *Research Letters*, 30(10):n/a–n/a. 1529.
- 556 Schulz, M. and Lanzerotti, L. J. (1974). *Particle Diffusion in the Radiation Belts*.
 557 Springer.
- 558 Seppälä, A., Douma, E., Rodger, C., Verronen, P., Clilverd, M. A., and Bortnik, J.
 559 (2018). Relativistic electron microburst events: Modeling the atmospheric impact.
 560 *Geophysical Research Letters*, 45(2):1141–1147.

- 561 Spence, H. E., Blake, J. B., Crew, A. B., Driscoll, S., Klumpar, D. M., Larsen,
 562 B. A., Legere, J., Longworth, S., Mosleh, E., O'Brien, T. P., Smith, S., Springer,
 563 L., and Widholm, M. (2012). Focusing on size and energy dependence of electron
 564 microbursts from the van allen radiation belts. *Space Weather*, 10(11).
- 565 Summers, D. (2005). Quasi-linear diffusion coefficients for field-aligned electro-
 566 magnetic waves with applications to the magnetosphere. *Journal of Geophysical
 567 Research: Space Physics*, 110(A8):n/a–n/a. A08213.
- 568 Summers, D., Thorne, R. M., and Xiao, F. (1998). Relativistic theory of wave-particle
 569 resonant diffusion with application to electron acceleration in the magnetosphere.
 570 *Journal of Geophysical Research: Space Physics*, 103(A9):20487–20500.
- 571 Thorne, R. M., O'Brien, T. P., Shprits, Y. Y., Summers, D., and Horne, R. B. (2005).
 572 Timescale for MeV electron microburst loss during geomagnetic storms. *Journal
 573 of Geophysical Research: Space Physics*, 110(A9). A09202.
- 574 Trefall, H., Bjordal, J., Ullaland, S., and Stadsnes, J. (1966). On the extension of
 575 auroral-zone x-ray microbursts. *Journal of Atmospheric and Terrestrial Physics*,
 576 28(2):225–233.
- 577 Tsurutani, B. T. and Lakhina, G. S. (1997). Some basic concepts of wave-particle
 578 interactions in collisionless plasmas. *Reviews of Geophysics*, 35(4):491–501.
- 579 Ukhorskiy, A. Y., Anderson, B. J., Brandt, P. C., and Tsyganenko, N. A. (2006).
 580 Storm time evolution of the outer radiation belt: Transport and losses. *Journal of
 581 Geophysical Research: Space Physics*, 111(A11):n/a–n/a. A11S03.
- 582 Van Allen, J. A. (1959). The geomagnetically trapped corpuscular radiation. *Journal
 583 of Geophysical Research*, 64(11):1683–1689.
- 584 Vernov, S. and Chudakov, A. (1960). Investigation of radiation in outer space. In
 585 *International Cosmic Ray Conference*, volume 3, page 19.
- 586 Walker, A. D. M. (1993). *Plasma waves in the magnetosphere*, volume 24. Springer
 587 Science & Business Media.